

Demonstration of Scale-Invariant Rayleigh-Taylor Instability Growth in Laser-Driven Cylindrical Implosion Experiments

J. P. Sauppe^{1,*}, S. Palaniyappan¹, B. J. Tobias¹, J. L. Kline¹, K. A. Flipppo¹, O. L. Landen², D. Shvarts^{3,4}, S. H. Batha¹, P. A. Bradley¹, E. N. Loomis¹, N. N. Vazirani¹, C. F. Kawaguchi¹, L. Kot¹, D. W. Schmidt¹, T. H. Day¹, A. B. Zylstra² and E. Malka⁴

¹Los Alamos National Laboratory, P.O. Box 1663, Los Alamos, New Mexico 87545, USA

²Lawrence Livermore National Laboratory, Livermore, California 94550, USA

³Ben-Gurion University of the Negev, Beersheba, 8410501, Israel

⁴Nuclear Research Center of the Negev, Beersheba, 84190, Israel

 (Received 20 December 2019; revised manuscript received 16 March 2020; accepted 7 April 2020; published 7 May 2020)

Rayleigh-Taylor instability growth is shown to be hydrodynamically scale invariant in convergent cylindrical implosions for targets that varied in radial dimension and implosion timescale by a factor of 3. The targets were driven directly by laser irradiation providing a short impulse, and instability growth at an embedded aluminum interface occurs as it converges radially inward by a factor of 2.25 and decelerates on a central foam core. Late-time growth factors of 14 are observed for a single-mode $m = 20$ azimuthal perturbation at both scales, despite the differences in laser drive conditions between the experimental facilities, consistent with predictions from radiation-hydrodynamics simulations. This platform enables detailed investigations into the limits of hydrodynamic scaling in high-energy-density systems.

DOI: [10.1103/PhysRevLett.124.185003](https://doi.org/10.1103/PhysRevLett.124.185003)

Introduction.—The goal of inertial confinement fusion (ICF) is to compress and heat deuterium-tritium (DT) fuel to conditions where the isotopes fuse and release energy [1]. Compression is achieved by ablating a shell that encapsulates the DT, imploding the fuel via the rocket effect. The direct-drive approach uses lasers to directly irradiate the capsule and operates at a convergence ratio (CR, initial radius/final radius) of roughly 17–23 [2]. The indirect-drive route uses x rays produced by illuminating the inner walls of a hohlraum to drive the ablation [3], with capsules designed around a CR of 25–35 [4] to achieve conditions necessary for ignition and burn of the fuel. The layered designs of ICF capsules provide many interfaces where hydrodynamic instabilities can grow through Rayleigh-Taylor [5,6] and Richtmyer-Meshkov [7,8] processes, and these are further modified in convergent geometry through Bell-Plesset (BP) effects [9,10]. At these high convergence ratios, ICF implosions are extremely susceptible to hydrodynamic instability growth. The failure of many capsules designed to ignite on the National Ignition Facility (NIF) [11] has been attributed to these instabilities mixing unablated shell material into the fuel [12]. This mixing effectively reduces the energy delivered to the central hot spot region needed to initiate thermonuclear burn, necessitating a larger driver energy to compensate for these inefficiencies. The size and type of this larger driver and the designs for ICF capsules that utilize it remain areas of active investigation.

Designs for larger capsules often leverage hydrodynamic scaling [13], which is the approach that has been used as

direct-drive target designs are scaled from the 30 kJ OMEGA laser facility [14] up to the 1.8 MJ NIF [15,16]. Hydrodynamic scaling is motivated by the fact that the Euler equations are invariant to the transformation $\mathbf{x} \rightarrow \lambda\mathbf{x}$ and $t \rightarrow \lambda t$ [17,18]. As a result, increasing the size of the target by a factor of λ and modifying the drive pulse so that the implosion velocity is constant (drawing out the timescales by the same factor of λ) leaves the hydrodynamic behavior unchanged. It is important to note that other physical processes are not scale invariant, such as heat conduction, viscosity, kinetic effects, and laser plasma interactions, which are very important in traditional ICF implosions [13] and must be accounted for accordingly. In particular, recent work highlights how Rayleigh-Taylor instability growth during the deceleration phase is expected to differ for capsules designed for OMEGA and the NIF [19] as a result of ablative stabilization from the hot spot. There are also differences in the laser drivers at OMEGA and the NIF (i.e., beam sizes, number of beams, pointings, and phase plates) that make a direct scaling of platforms between these facilities more challenging. Similar efforts are under way for scaling of indirect-drive designs at the NIF. State-of-the-art simulations that have been tuned to match experimental observables at the NIF scale are being used to estimate the required driver energy needed for ignition [20,21]. Experimentally, high-density carbon targets have been successfully scaled from $0.8\times$ up to the full NIF $1.0\times$ scale [22], and a model for fuel-ablator mix tested for subscale beryllium capsules predicts less performance

degradation as capsule size is increased [23], but extrapolations to larger changes in scale remain untested.

Here, for the first time, we report on a cylindrical implosion platform that directly demonstrates instability growth that is scale invariant over a factor of 3 increase in radial dimension and implosion timescale in the high-energy-density (HED) regime. These results are directly relevant for scaling to next generation ICF facilities, with capsule designs that are 2–4 times larger than current NIF-scale capsules [24]. They also represent the first HED experiments to directly measure deceleration phase Rayleigh-Taylor instability in convergent cylindrical geometry. Spherical experiments have measured growth indirectly during the deceleration phase [25,26], but cylindrical systems have the advantage that direct measurements of the instability growth can be made viewing down the axis. Cylinders incorporate all of the effects of convergence that occur in spherical systems [27], albeit at lower order in r , and they have been successfully fielded in many past experiments [28–32]. Although cylinders result in less compression than spherical implosions, the open axial ends allow for the possibility of auxiliary heating schemes, as in the MagLIF concept [33]. This could partially offset the lower expected central temperatures that arise from end losses in the cylindrical system. The relatively simple nature of the short, impulsive laser drive used in this work relaxes the nonscaling constraints, which here arise primarily from different density scale lengths and evolution timescales in the coronal plasma. This provides a target design that is amenable to hydroscaling, though more complicated drive pulses could be considered. The platform enables detailed studies that leverage the higher data return of the OMEGA laser facility to improve statistics, while utilizing the laser energy and power of the NIF to drive larger targets to higher convergence ratios with final feature sizes that remain measurable. Future work will focus on achieving a CR of 10–17, where BP effects are more pronounced, a necessary but not sufficient condition for surrogacy to ICF implosions. This will be directly applicable to indirectly driven double shell [34] and wetted foam targets [35], as well as direct-drive implosions. Further extensions to the cylindrical implosion platform will begin to examine the limits of hydrodynamic scale invariance in HED systems.

Target design.—The scale-1 targets, fielded at the OMEGA laser facility and shown in Fig. 1(a), are nominally 2500 μm long with an outer radius of 493 μm , based on previous cylindrical implosion experiments [31,32]. The outer portion of the target consists of an epoxy (CH) ablator (1.25 g/cm^3) that is 63 μm thick, with a nominal inner radius of 430 μm . A 500 μm long, 12 μm thick aluminum marker band (2.7 g/cm^3) is embedded in the center of the cylinder, such that the inner radius of the aluminum marker is nearly flush with the inner surface of the surrounding epoxy. The aluminum is opaque to backlighter x rays and is

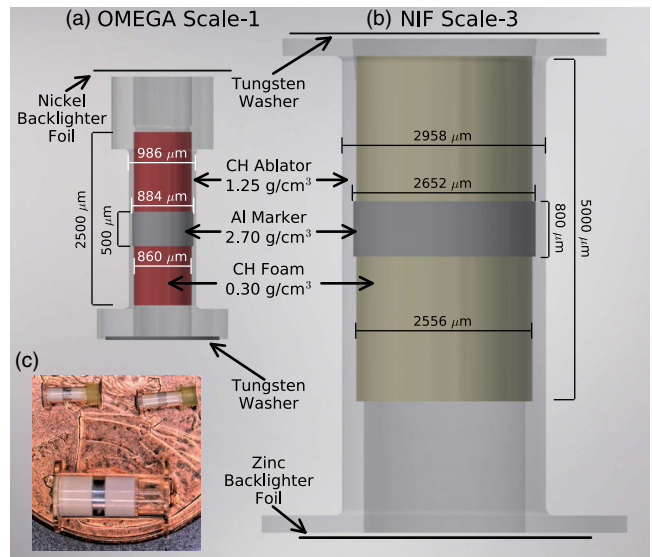


FIG. 1. (a) Schematic of the scale-1 cylindrical target fielded at OMEGA and (b) the scale-3 target fielded at the NIF. (c) Two OMEGA targets (top) and one NIF target (bottom) on the surface of a penny.

used to provide radiographic contrast. The cylinder is filled with a 300 mg/cm^3 CH foam with an outer radius of 425 μm , leaving only a small gap between the foam and the inner surfaces of both the epoxy and the marker. The deceleration profile and final convergence of the marker can be controlled by changing the density of the central foam. The marker has been thickened up slightly and the foam density has increased from the numbers reported in Ref. [36]. A prescribed initial perturbation is machined on the inner surface of the aluminum, providing a seed for hydrodynamic instability growth as the target implodes. Here, we focus on a single $m = 20$ azimuthal mode, since BP effects vanish in cylindrical geometry for $m = 0$ [37], with an initial amplitude of 4 μm for the scale-1 targets. This was selected as a balance between high mode numbers (which have more growth [38]), fabricability, and ability to image instability growth in the presence of parallax effects.

The scale-3 cylindrical targets for the NIF have an outer ablator radius of 1479 μm , an inner ablator radius of 1290 μm , a 36 μm thick aluminum marker embedded in the inner surface of the ablator, and a central foam cylinder with an outer radius of 1278 μm . The $m = 20$ perturbation on the inner surface of the aluminum marker has an amplitude of 12 μm for the NIF-scale targets. For practical reasons, the target length is not scaled by the same factor as the radius, as shown in Fig. 1(b). In the NIF-scale targets, the marker length is increased to 800 μm , and the total target length is increased to 5000 μm (excluding the supports for the backlighter mount, which are integral to the target). Since the laser energy scales as the surface area, reducing the illuminated length reduces the required laser energy while keeping the marker region uniform during the implosion.

The experiments are imaged by illuminating a backlighter foil attached to one end of the cylindrical target, producing x rays that travel down the cylinder axis. The OMEGA targets use a nickel foil with dominant He- α emission at 7.8 keV, while the NIF targets use a zinc foil with emission at 8.9 keV to compensate for signal loss through the increased length. For cold aluminum at 2.7 g/cm^3 , the product of the linear absorption coefficient for the backlighter energy times the length of the aluminum marker differs by less than 10% between the two scales. The marker is opaque to the backlighter x rays, allowing for direct measurements of instability growth at the interior and exterior marker interfaces at various times during the implosion. Sixteen different times are imaged in each experimental shot by filtering the x rays through a pinhole array before passing onto a time-gated framing camera. A circular tungsten washer placed at the opposite end of the cylinder from the backlighter foil prevents cross talk between different pinhole images by eliminating x-ray transmission except through the central hole of the washer, with a nominal inner radius of $375 \text{ }\mu\text{m}$ at OMEGA and $1125 \text{ }\mu\text{m}$ at the NIF.

Experimental setup.—At OMEGA, the cylindrical target is driven with 40 laser beams using SG5 phase plates in a 1 ns Gaussian square pulse with a prescribed total energy of 18 kJ. The beams are offset from the target chamber center $\pm 200 \text{ }\mu\text{m}$ along the cylinder axis to provide a nearly flat illumination pattern across the central region containing the marker band, and the view factor code VISRAD [39] finds a peak intensity of $4 \times 10^{14} \text{ W/cm}^2$ on the cylinder surface. Radiation-hydrodynamics modeling using the xRAGE [40] code predicts that the marker implodes in an axially uniform manner, and this is supported by radiographic images taken from a transverse view of the cylinder during the implosion. xRAGE has recently been updated to include physics necessary for properly simulating ICF and HED experiments [41], including three-temperature (electron, ion, radiation) modeling and a new laser package [42], and it has shown very favorable agreement when modeling previous cylindrical implosion experiments [43]. The length of the laser pulse and target dimensions are chosen such that the laser drive turns off as the shock breaks out of the inner surface of the aluminum marker. Following shock breakout and a brief period of Richtmyer-Meshkov growth, the aluminum marker begins moving inward at around $65 \text{ }\mu\text{m/ns}$. As the marker compresses the central foam, a period of slow ($\approx 5 \text{ }\mu\text{m/ns}^2$) deceleration phase Rayleigh-Taylor growth begins. The deceleration here is similar to the continuous deceleration phase of an ICF implosion [44], though the magnitude is considerably lower. The marker coasts inward to a final convergence ratio of 2.25 before being struck by the shock rebounding from the cylinder axis.

The 192 laser beams of the NIF, designed for indirect-drive ICF, are arranged into 48 quads (sets of four beams),

which are further split into inner and outer cones. The inner cones consist of 4 quads at 23.5° and 4 quads at 30° , each relative to the hohlraum axis of rotation, while the outer cones consist of 8 quads at 44.5° and another 8 quads at 50° . For our directly driven cylindrical implosion experiments, the 44.5° and 50.0° beams are used to drive the cylinder, and the 23.5° and 30.0° beams from the lower hemisphere are used to drive the backlighter. VISRAD predicts a narrow initial intensity pattern peaked at $6.5 \times 10^{14} \text{ W/cm}^2$ over the marker layer, but this does not account for the angular dependence of laser absorption [45] or how the absorption changes as the coronal plasma evolves. Instead, we use xRAGE simulations with parameters calibrated from the OMEGA-scale implosions to determine the optimal drive conditions for the NIF-scale targets. The beam pointings are chosen to give an axially uniform implosion of the marker layer: the southern hemisphere drive beams are offset toward the north pole by $1035 \text{ }\mu\text{m}$, and the northern hemisphere beams are offset the same amount toward the south pole. Hydrosaling according to $\mathbf{x} \rightarrow \lambda \mathbf{x}$ and $t \rightarrow \lambda t$ necessitates that the laser pulse is 3 ns long. The power (0.589 TW/beam) was chosen such that the NIF-scale marker trajectory implodes with the same velocity as the OMEGA-scale trajectory, with nearly identical ablation pressures of roughly 40 Mbar, in preshot simulations. The 128 drive beams deliver a total of 226 kJ of laser energy to the target, allowing for even larger cylinders to be fielded at the NIF in the future. Simulations suggest that a scale-4 cylinder could be driven along a scale-invariant trajectory with 614 kJ in a 4 ns pulse, though the higher initial laser intensities require further investigation to assess the efficacy of coupling this energy to the target.

Results.—The initial sinusoidal perturbation on the inner surface of the aluminum marker layer grows considerably during the implosion and develops the classic bubble and spike features of late-time Rayleigh-Taylor instability, as can be seen from the radiographic data from one of the 16 frames for the OMEGA and NIF experiments shown in Figs. 2(a) and 2(b), respectively. The OMEGA data are shown roughly 6.2 ns after the start of the 1 ns drive, while the NIF data are shown at the corresponding hydroscaled time of 18.6 ns after the start of the 3 ns drive. Mushroom heads are just beginning to develop at the tips of the spikes at these image times. The shock position is also evident in the CH foam, as the unshocked foam is more transparent to the backlighter x rays. These two images are just prior to shock collapse on the cylinder axis. When the shock rebounds, it recompresses the CH foam, further lowering the transmission and allowing extraction of the entire shock trajectory. Linear theory [46] predicts that instability growth here occurs in the strongly driven limit, with only modest contributions due to convergence, but it is hoped that these results will spur further interest in extending theories of instability growth in convergent geometry beyond current limits [47–49].

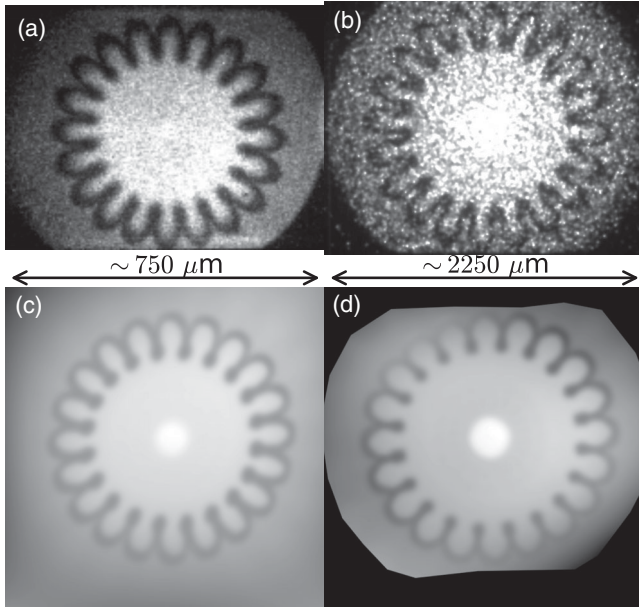


FIG. 2. Experimental radiographs from (a) OMEGA shot 93069 and (b) NIF shot N190212-003. Synthetic radiographs from *xRAGE* simulations of (c) OMEGA shot 93069 and (d) NIF shot N190212-003, including parallax and pinhole blurring.

Synthetic radiographs reproduce many features of the experimental radiographs, as can be seen in Figs. 2(c) and 2(d) for the OMEGA- and NIF-scale simulations. Appropriate pinhole blurring and the effects of image parallax are included, but the illumination pattern on the backlighter is not modeled. (Features are extracted from extrema in gradients of transmission, so this is not expected to be important.) The marker layer appears slightly thicker in the experimental radiographs than in the synthetic radiographs. This could be explained by either a modest bowing that is not captured in these 2D simulations, high mode instabilities contributing to additional mixing of the layer, or preheat (which is not currently modeled in these simulations) depositing additional energy into the aluminum early in time. These three possibilities are under active investigation. The latter two are important in their own right for ICF, and the cylindrical implosion platform provides a complementary method of investigating these effects from spherical implosions.

The experimental trajectories are qualitatively similar between the OMEGA- and NIF-scale targets, as can be seen in Fig. 3(a), which shows several key features extracted from the radiographs and plotted versus scaled radius r/λ and scaled time t/λ ($\lambda = 1$ for OMEGA and $\lambda = 3$ for NIF). In order of decreasing radial position, the features are the outermost surface of the aluminum marker, the bubble pocket position, the spike tip position, and the shock front. The shock trajectory agrees with the self-similar converging shock solution in cylindrical geometry [17], though the NIF trajectories (x's) lag slightly behind the OMEGA

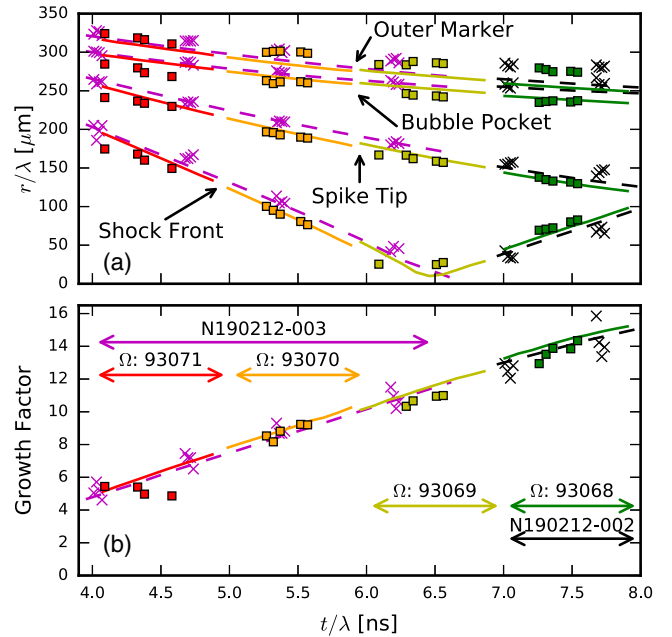


FIG. 3. (a) Trajectories extracted from experimental radiographs (OMEGA, squares; NIF, x's) compared to postshot *xRAGE* predictions (OMEGA, solid lines; NIF, dashed lines). Clustered NIF data represent 4 frames from a single strip, and uncertainty due to azimuthal variations is on the order of the marker size. The scatter of OMEGA data about the apparent trends is about 6%–7%, but the data are too statistically limited to represent a confidence interval. Future work will further reduce this by introducing temporal constraints into the analysis. (b) Growth factor for OMEGA and NIF shots compared to postshot *xRAGE* predictions (lines).

data (squares). This may be partially attributed to the slightly less effective coupling of the laser energy to the hydrodynamic motion of the target. The design work assumed that the same coupling efficiency of laser energy to target motion occurred at OMEGA and the NIF, but postshot simulations indicate this is not the case. The NIF targets are also not exactly hydroscaled, due to fabrication constraints: the radii are within 1% of nominal values, but the thickness of the aluminum marker differed by as much as 15% from nominal.

Trajectories extracted from the *xRAGE* simulations match the experimental measurements well, as can be seen in the solid (OMEGA) and dashed (NIF) lines overlaid in Fig. 3. Each experimental shot is simulated separately using the as-built target dimensions and the as-fired laser pulse. Our simulations include an *ad hoc* laser power multiplier that attempts to account for cross-beam energy transfer [50] and other laser plasma instabilities that are not presently modeled. (A cross-beam energy transfer model has been implemented in *xRAGE* and is being tested against these data now.) The power multiplier η_{laser} is tuned in the postshot simulations in order to match the experimentally measured trajectories. The OMEGA simulations use

$\eta_{\text{laser}} = 0.85$, while the NIF cases use $\eta_{\text{laser}} = 0.75$. The lower power multiplier for the NIF-scale targets is attributed to the higher intensity and the longer pulse length used. The use of a constant-in-time multiplier is believed acceptable, as the drive ends before the marker begins to move; more complicated pulse shapes will likely require more sophisticated models.

The OMEGA and NIF experiments show peak growth factors around 14 at $t/\lambda \sim 7.7$ ns, just before the rebounding shock hits the marker, as can be seen in Fig. 3(b). The mode amplitude is inferred by taking half of the distance between the extracted bubble pocket and spike tip positions, and the growth factor is this value divided by the initial perturbation amplitude, as determined from detailed target metrology. Growth factors from the xRAGE simulations, also shown in Fig. 3(b), predict scale-invariant growth between the OMEGA and NIF targets, in agreement with the experimental measurements. Lastly, note that the mode continues to exhibit growth when the wave-number-amplitude product, $ka_m = ma_m/r$, is greater than order unity, which is consistent with previous findings [31].

We developed a cylindrical implosion platform that is hydrodynamically scale invariant over a factor of 3 increase in radial dimension and implosion timescale. Experiments fielded at both the OMEGA laser facility and the NIF measuring Rayleigh-Taylor instability growth during deceleration find instability growth factors of 14 at a CR of 2.25, in agreement with xRAGE radiation-hydrodynamics predictions. The scale-invariant nature of the hydrodynamics in this platform enables detailed cross comparisons to be made between many small targets fielded at OMEGA and a handful of larger targets fielded at the NIF, allowing large statistically significant datasets to be leveraged in hydrodynamics studies in a convergent geometry. Near term efforts will focus on extending the platform to higher convergence ratios through a combination of lower density foams or gas fills and alterations in the laser drive, and we have begun to examine multi-mode initial conditions and surface roughness in preliminary work at OMEGA. Further extensions will examine the breakdown of hydrodynamic scale invariance in HED systems, such as the predicted differences in ablative stabilization during deceleration [19].

The authors are grateful to the University of Rochester's Laboratory for Laser Energetics and to the Lawrence Livermore National Laboratory's NIF operations team for help fielding the experiments. The NIF experimental shots were awarded through the Discovery Science program. This work used resources provided by Los Alamos National Laboratory, supported by the U.S. Department of Energy National Nuclear Security Administration, operated by Triad National Security, LLC (Contract No. 89233218CNA000001).

- *jpsauppe@lanl.gov
- [1] J. Nuckolls, L. Wood, A. Thiessen, and G. Zimmerman, *Nature (London)* **239**, 139 (1972).
 - [2] S. Regan, V. Goncharov, I. Igumenshchev, T. Sangster, R. Betti, A. Bose, T. Boehly, M. Bonino, E. Campbell, D. Cao *et al.*, *Phys. Rev. Lett.* **117**, 025001 (2016).
 - [3] J. Lindl, *Phys. Plasmas* **2**, 3933 (1995).
 - [4] N. Meezan, M. Edwards, O. Hurricane, P. Patel, D. Callahan, W. Hsing, R. Town, F. Albert, P. Amendt, L. B. Hopkins *et al.*, *Plasma Phys. Controlled Fusion* **59**, 014021 (2017).
 - [5] L. Rayleigh, *Proc. London Math. Soc.* **s1-14**, 170 (1882).
 - [6] G. I. Taylor, *Proc. R. Soc. Ser. A* **201**, 192 (1950).
 - [7] R. D. Richtmyer, *Commun. Pure Appl. Math.* **13**, 297 (1960).
 - [8] E. Meshkov, *Fluid Dyn.* **4**, 101 (1972).
 - [9] G. I. Bell, Technical Report No. LA-1321, Los Alamos Scientific Laboratory, 1951.
 - [10] M. S. Plesset, *J. Appl. Phys.* **25**, 96 (1954).
 - [11] E. I. Moses, *Nucl. Fusion* **49**, 104022 (2009).
 - [12] J. Lindl, O. Landen, J. Edwards, E. Moses, and NIC Team, *Phys. Plasmas* **21**, 020501 (2014).
 - [13] R. Nora, R. Betti, K. Anderson, A. Shvydky, A. Bose, K. Woo, A. Christopherson, J. Marozas, T. Collins, P. Radha *et al.*, *Phys. Plasmas* **21**, 056316 (2014).
 - [14] T. Boehly, D. Brown, R. Craxton, R. Keck, J. Knauer, J. Kelly, T. Kessler, S. Kumpan, S. Loucks, S. Letzring *et al.*, *Opt. Commun.* **133**, 495 (1997).
 - [15] V. Goncharov, T. Sangster, R. Betti, T. Boehly, M. Bonino, T. Collins, R. Craxton, J. Delettrez, D. Edgell, R. Epstein *et al.*, *Phys. Plasmas* **21**, 056315 (2014).
 - [16] S. Regan, V. Goncharov, T. Sangster, E. Campbell, R. Betti, K. Anderson, T. Bernat, A. Bose, T. Boehly, M. Bonino *et al.*, *Fusion Sci. Technol.* **73**, 89 (2018).
 - [17] Y. B. Zel'dovich and Y. P. Raizer, *Physics of Shock Waves and High-Temperature Hydrodynamic Phenomena* (Academic Press, New York, 1966).
 - [18] D. Ryutov, R. Drake, J. Kane, E. Liang, B. Remington, and W. Wood-Vasey, *Astrophys. J.* **518**, 821 (1999).
 - [19] A. Bose, K. Woo, R. Nora, and R. Betti, *Phys. Plasmas* **22**, 072702 (2015).
 - [20] D. Clark, C. Weber, A. Kritcher, J. Milovich, P. Patel, S. Haan, B. Hammel, J. Koning, M. Marinak, M. Patel *et al.*, *Nucl. Fusion* **59**, 032008 (2019).
 - [21] D. Clark, C. Weber, J. Milovich, A. Pak, D. Casey, B. Hammel, D. Ho, O. Jones, J. Koning, A. Kritcher *et al.*, *Phys. Plasmas* **26**, 050601 (2019).
 - [22] D. Casey, C. Thomas, K. Baker, B. Spears, M. Hohenberger, S. Khan, R. Nora, C. Weber, D. Woods, O. Hurricane *et al.*, *Phys. Plasmas* **25**, 056308 (2018).
 - [23] A. Zylstra, S. Maclaren, S. Yi, J. Kline, D. Callahan, O. Hurricane, B. Bachmann, G. Kyrala, L. Masse, P. Patel *et al.*, *Phys. Plasmas* **26**, 052707 (2019).
 - [24] R. Olson, G. Chandler, M. Derzon, D. Hebron, J. Lash, R. Leeper, T. Nash, G. Rochau, T. Sanford, N. Alexander *et al.*, *Fusion Sci. Technol.* **35**, 260 (1999).
 - [25] V. Smalyuk, J. Delettrez, V. Goncharov, F. Marshall, D. Meyerhofer, S. Regan, T. Sangster, R. Town, and B. Yaakobi, *Phys. Plasmas* **9**, 2738 (2002).

- [26] L. Pickworth, B. Hammel, V. Smalyuk, H. Robey, L. Benedetti, L. Berzak Hopkins, D. Bradley, J. Field, S. Haan, R. Hatarik *et al.*, *Phys. Plasmas* **25**, 054502 (2018).
- [27] K. O. Mikaelian, *Phys. Fluids* **17**, 094105 (2005).
- [28] W. W. Hsing and N. M. Hoffman, *Phys. Rev. Lett.* **78**, 3876 (1997).
- [29] D. L. Tubbs, C. W. Barnes, J. B. Beck, N. M. Hoffman, J. A. Oertel, R. G. Watt, T. Boehly, D. Bradley, P. Jaanimagi, and J. Knauer, *Phys. Plasmas* **6**, 2095 (1999).
- [30] C. W. Barnes, S. Batha, A. Dunne, G. Magelssen, S. Rothman, R. Day, N. Elliott, D. Haynes, R. Holmes, J. Scott *et al.*, *Phys. Plasmas* **9**, 4431 (2002).
- [31] J. R. Fincke, N. E. Lanier, S. H. Batha, R. M. Hueckstaedt, G. R. Magelssen, S. D. Rothman, K. W. Parker, and C. J. Horsfield, *Phys. Rev. Lett.* **93**, 115003 (2004).
- [32] N. Lanier, G. Magelssen, S. Batha, J. Fincke, C. Horsfield, K. Parker, and S. Rothman, *Phys. Plasmas* **13**, 042703 (2006).
- [33] M. R. Gomez, S. A. Slutz, A. B. Sefkow, D. B. Sinars, K. D. Hahn, S. B. Hansen, E. C. Harding, P. F. Knapp, P. F. Schmit, C. A. Jennings *et al.*, *Phys. Rev. Lett.* **113**, 155003 (2014).
- [34] D. Montgomery, W. Daughton, B. Albright, A. Simakov, D. Wilson, E. Dodd, R. Kirkpatrick, R. Watt, M. Gunderson, E. Loomis *et al.*, *Phys. Plasmas* **25**, 092706 (2018).
- [35] R. E. Olson, R. J. Leeper, J. L. Kline, A. B. Zylstra, S. A. Yi, J. Biener, T. Braun, B. J. Koziowski, J. D. Sater, P. A. Bradley *et al.*, *Phys. Rev. Lett.* **117**, 245001 (2016).
- [36] J. P. Sauppe, S. Palaniyappan, E. N. Loomis, J. L. Kline, K. A. Flippo, and B. Srinivasan, *Matter Radiat. Extremes* **4**, 065403 (2019).
- [37] A. Velikovich and P. Schmit, *Phys. Plasmas* **22**, 122711 (2015).
- [38] J. D. Lindl, P. Amendt, R. L. Berger, S. G. Glendinning, S. H. Glenzer, S. W. Haan, R. L. Kauffman, O. L. Landen, and L. J. Suter, *Phys. Plasmas* **11**, 339 (2004).
- [39] J. MacFarlane, *J. Quant. Spectrosc. Radiat. Transfer* **81**, 287 (2003).
- [40] M. Gittings, R. Weaver, M. Clover, T. Betlach, N. Byrne, R. Coker, E. Dendy, R. Hueckstaedt, K. New, W. R. Oakes *et al.*, *Comput. Sci. Discovery* **1**, 015005 (2008).
- [41] B. M. Haines, C. Aldrich, J. M. Campbell, R. M. Rauenzahn, and C. A. Wingate, *Phys. Plasmas* **24**, 052701 (2017).
- [42] J. Marozas, M. Hohenberger, M. Rosenberg, D. Turnbull, T. Collins, P. Radha, P. McKenty, J. Zuegel, F. Marshall, S. Regan *et al.*, *Phys. Plasmas* **25**, 056314 (2018).
- [43] J. P. Sauppe, B. M. Haines, S. Palaniyappan, P. A. Bradley, S. H. Batha, E. N. Loomis, and J. L. Kline, *Phys. Plasmas* **26**, 042701 (2019).
- [44] R. Betti, K. Anderson, V. Goncharov, R. McCrory, D. Meyerhofer, S. Skupsky, and R. Town, *Phys. Plasmas* **9**, 2277 (2002).
- [45] B. Scheiner and M. Schmitt, *Phys. Plasmas* **26**, 024502 (2019).
- [46] R. Epstein, *Phys. Plasmas* **11**, 5114 (2004).
- [47] M. Vandenboomgaerde, P. Rouzier, D. Souffland, L. Biamino, G. Jourdan, L. Houas, and C. Mariani, *Phys. Rev. Fluids* **3**, 014001 (2018).
- [48] L. Wang, J. Wu, H. Guo, W. Ye, J. Liu, W. Zhang, and X. He, *Phys. Plasmas* **22**, 082702 (2015).
- [49] K. Zhao, C. Xue, L. Wang, W. Ye, J. Wu, Y. Ding, W. Zhang, and X. He, *Phys. Plasmas* **25**, 092703 (2018).
- [50] I. Igumenshchev, D. Edgell, V. Goncharov, J. Delettrez, A. Maximov, J. Myatt, W. Seka, A. Shvydky, S. Skupsky, and C. Stoeckl, *Phys. Plasmas* **17**, 122708 (2010).